



AALBORG UNIVERSITY
DENMARK

Aalborg Universitet

Analyses and Full-Duplex Applications of Circularly Polarized OAM Arrays Using Sequentially Rotated Configuration

Zhang, Yiming; Li, Jia-Lin

Published in:
IEEE Transactions on Antennas and Propagation

DOI (link to publication from Publisher):
[10.1109/TAP.2018.2872169](https://doi.org/10.1109/TAP.2018.2872169)

Publication date:
2018

[Link to publication from Aalborg University](#)

Citation for published version (APA):
Zhang, Y., & Li, J-L. (2018). Analyses and Full-Duplex Applications of Circularly Polarized OAM Arrays Using Sequentially Rotated Configuration. *IEEE Transactions on Antennas and Propagation*, 7010-7020.
<https://doi.org/10.1109/TAP.2018.2872169>

General rights

Copyright and moral rights for the publications made accessible in the public portal are retained by the authors and/or other copyright owners and it is a condition of accessing publications that users recognise and abide by the legal requirements associated with these rights.

- Users may download and print one copy of any publication from the public portal for the purpose of private study or research.
- You may not further distribute the material or use it for any profit-making activity or commercial gain
- You may freely distribute the URL identifying the publication in the public portal -

Take down policy

If you believe that this document breaches copyright please contact us at vbn@aub.aau.dk providing details, and we will remove access to the work immediately and investigate your claim.

Analyses and Full-Duplex Applications of Circularly Polarized OAM Arrays Using Sequentially Rotated Configuration

Yi-Ming Zhang¹, Student Member, IEEE, and Jia-Lin Li¹

Abstract—This paper presents the analyses of circularly polarized orbital angular momentum (OAM) ring arrays using sequentially rotated configurations. For the studied OAM-based microstrip antenna arrays, the relationship between the excitation settings and the generated OAM modes are studied together with the axial ratio (AR) bandwidths at the beam maximums. Furthermore, a dual-OAM-mode circularly polarized array is proposed for full-duplex applications. Based on the presented OAM-mode selection method, the self-interference due to the strong mutual coupling within the array can be well canceled, leading to a high interport isolation. A demonstrator centered at 15 GHz with OAM modes of +1 and +2 is developed and fabricated for verification purposes. The demonstrator uses a sharing antenna scheme for the two OAM modes to realize a compact architecture. Measured results indicate that the demonstrator characterizes good interport isolation within a wide bandwidth from 13.92 to 16.38 GHz referring to a 45 dB level as well as wide AR bandwidths at the beam maximums.

Index Terms—Full duplex, orbital angular momentum (OAM), self-interference suppression, sequentially rotated configuration.

I. INTRODUCTION

WITH the ever-decreasing available spectrum for future wireless communications, the study of full-duplex architectures has drawn increasing attention. For a full-duplex system, a single channel is employed for bidirectional communications simultaneously, leading to a doubled spectrum efficiency compared to half-duplex operations theoretically [1]–[4]. To realize a full-duplex system, a key challenge lies in the suppression of the strong self-interference leakage from the transmitter (Tx) to the local receiver (Rx), where the leakage mainly arises from the coupling at the antenna level [1], [2]. Otherwise, the received signals would drown in the self-interference noise, making it difficult even impossible work for the Rx. For a single-antenna scenario, high isolations between the local Tx and Rx can be readily achieved by using dual-polarized schemes [3], [4], but they could not

approach to suppress the self-interference with antenna-array-based systems due to the complicated mutual coupling among antenna elements.

Recently, orbital angular momentum (OAM) waves, featuring helical phase fronts and amplitude nulls at beam center, as well as orthogonality among different OAM modes, have attracted lots of interest for improving the spectrum utilization [5]–[16]. Based on some recent studies [11]–[13], it is believed that the OAM-based wireless communication is a specified subset of the multiple-in multiple-out-based technique. Particularly, several studies indicate that the OAM wave presents a potential insight to deal with the self-interference suppression for full-duplex applications [6]–[8]. Moreover, it is potential and attractive to further improve the spectrum efficiency and data rate of a full-duplex system by using multi-OAM-mode configurations for both uplink and downlink. In [6], OAM-based multiplexing experiments verified that the system capacity and spectrum efficiency of wireless communication links were increased by transmitting multiple coaxial data streams, where the achieved link isolations were of 16–26 dB. In [7], a dual-polarized microstrip antenna array was proposed for dual-OAM-mode applications with an interport isolation of 25 dB. These studies reveal that for full-duplex applications, self-interference suppression can benefit from the utilization of OAM-based schemes. However, the achieved suppressions are generally low since the self-interference owing to the mutual coupling among antennas is not well suppressed.

As for the self-interference suppression of an OAM-based full-duplex system, its basic and important issue is the generation of the OAM-based carriers. To generate OAM in radio beams, a common method is the use of uniform circular arrays (UCAs) [10], [11], [14]–[19]. In [14], a circular horn array was developed to generate OAM beams with three polarizations, two orthogonally linear polarizations (LPs), and one circular polarization (CP). In [15], an array consisting of eight CP patch antennas was designed under multi-OAM modes. In these studies, all antenna elements were positioned around a ring and excited under the arranged phases in a step of $2\pi l/N$, where N was the total element number and l was the excitation mode. As studied in [10], [11], and [14]–[16], the excitation mode l was defined as the OAM mode of the generated OAM waves. This is incontestable for the UCAs using nonsequentially rotated configurations. But for those

Manuscript received March 27, 2018; revised August 28, 2018; accepted September 12, 2018. Date of publication September 26, 2018; date of current version November 30, 2018. This work was supported by the Natural Science Foundation of China under Grant 61271025 and Grant 61601063. (Corresponding author: Jia-Lin Li).

The authors are with the School of Physics, University of Electronic Science and Technology of China, Chengdu 610054, China (e-mail: ymzhang@std.uestc.edu.cn; jialinli@uestc.edu.cn).

Color versions of one or more of the figures in this paper are available online at <http://ieeexplore.ieee.org>.

Digital Object Identifier 10.1109/TAP.2018.2872169

with sequentially rotated schemes, where each element is rotated around its own phase center with a phase step of $2\pi/N$ in φ -coordinate, the excitation mode l is not consequentially the OAM mode since the spatial phase distributions may be different for different antenna types [17]–[19]. For instance, OAM waves were generated using circular Vivaldi antenna array with the sequentially rotated configuration in [17], where the excitation mode l was the OAM mode. However, the study in [18] verified that for a sequentially rotated array composed of LP microstrip antennas, the excitation mode l was not the OAM mode. In [19], mechanically reconfigurable single-arm spiral antenna array was presented to generate CP OAM waves without using any phase shifting components ($l = 0$). On the other hand, for OAM-based wireless communications, a large aperture is generally required to effectively receive and demultiplex signals [20]–[23]. Recently, many efforts have been devoted to reduce the receiving aperture [24]–[27]. Studies indicate that a small receiving aperture located around the direction of maximal beams is feasible. This further indicates the radiation response, including the axial ratio (AR) performance of CP arrays at the beam maximum, is important.

In this paper, UCAs composed of CP microstrip antennas with sequentially rotated configurations to generate CP OAM waves are presented; the relationship between the OAM modes and the excitation phases of the array elements are further discussed. It is found that for the first time, using sequentially rotated array configuration provides a potential and attractive way to achieve a wide AR-bandwidth performance at the beam maximum. In addition, as compared with the non-sequentially rotated array, the rotational symmetry of the studied configuration could exhibit more regular mutual couplings within the array, thus could facilitate the suppression of the self-interference for full-duplex applications. Based on this, a dual-OAM-mode CP UCA scenario and its OAM-mode selection method for full-duplex applications are proposed and discussed, where the same CPs are utilized as the carriers for both Tx and Rx. For demonstration purposes, a prototype centered at 15 GHz is developed and fabricated. The measured and simulated results verify the proposed scheme behaves high interport isolations and wide AR bandwidths at the beam maximums.

II. ANALYSES OF OAM-BASED CIRCULARLY POLARIZED ARRAYS USING SEQUENTIALLY ROTATED CONFIGURATIONS

A. Analyses of the Excitation Modes and OAM Modes

Fig. 1(a) illustrates the configuration of the typically OAM-generating UCA, consisting of several CP antenna elements that are distributed equidistantly around the perimeter of a ring. The excitation phase of the n th element is given by [5]

$$\alpha_n = (n - 1)2\pi l/N, \quad n = 1, \dots, N \quad (1)$$

where l is the excitation mode and N is the total element number. It has been verified that for the scheme provided in Fig. 1(a), the generated OAM mode l_{OAM} equals to the excitation mode l , as discussed in [10], [11], and [14]–[16].

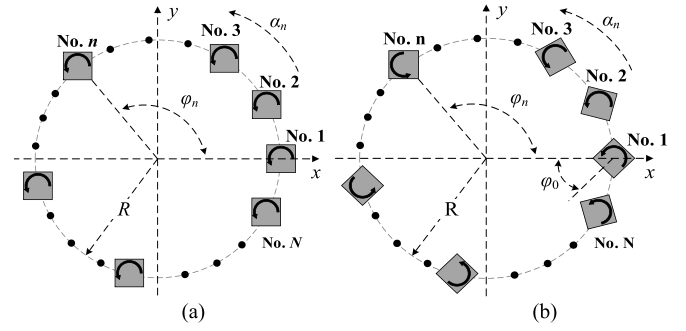


Fig. 1. Configurations of (a) typical UCA and (b) UCA with the sequentially rotated scheme.

In addition, the AR bandwidth is mainly determined by the performance of the antenna elements. Fig. 1(b) illustrates the configuration of the studied UCA with sequentially rotated CP elements; they are developed based on microstrip lines in this paper. The excitation phase in (1) is still applicable to the studied array. As discussed in Section I that for the studied scheme, the value of OAM mode, l_{OAM} , for the generated OAM wave is no longer consequentially equal to that of the excitation mode l . To further analyze the relationship between the values of l and l_{OAM} , numerical calculations are performed.

For a single CP microstrip element, it can be viewed as an array consisting of two orthogonal linearly polarized elements with a difference of excitation phase being $\pi/2$. Here, a numerical model for a linearly polarized microstrip antenna reported in [28] is employed. By multiplying with the array factor of the two-element array, the far-field components of the single CP microstrip antenna can be calculated, given as

$$E_\theta(\theta, \varphi) = E_0 \cos \varphi f(\theta, \varphi) + E_0 \cos(\varphi - \pi/2) f(\theta, \varphi - \pi/2) e^{j\varphi_0} \quad (2a)$$

$$E_\varphi(\theta, \varphi) = -E_0 \cos \theta \sin \varphi f(\theta, \varphi) - E_0 \cos \theta \sin(\varphi - \pi/2) f(\theta, \varphi - \pi/2) e^{j\varphi_0} \quad (2b)$$

$$f(\theta, \varphi) = \frac{\sin[\beta L \sin \theta \sin \varphi/2]}{\beta L \sin \theta \sin \varphi/2} \cos(\beta L \sin \theta \cos \varphi/2) \quad (2c)$$

$$L \approx 0.5\lambda_0/\sqrt{\varepsilon_r}, \quad -\pi/2 \leq \theta \leq \pi/2, \quad 0 \leq \varphi \leq 2\pi \quad (2d)$$

where $\varphi_0 = -\pi/2$ and $\varphi_0 = +\pi/2$ correspond to the right-hand circular polarization (RHCP) and left-hand circular polarization (LHCP), respectively; β is the phase constant in free space, λ_0 is the free-space wavelength at center frequency, L and ε_r are the side length of the square patch and the relative permittivity of the substrate, respectively. For the studied configuration shown in Fig. 1(b), the array factor is

$$S(\theta, \varphi) = \sum_{n=1}^N E(\theta, \varphi_n) e^{j[\beta R \sin \theta \cos \varphi_n + \alpha_n]} \quad (3a)$$

$$\varphi_n = \varphi - \varphi_n, \quad \varphi_n = (n - 1)2\pi/N \quad (3b)$$

where α_n is the excitation phase given in (1). By substituting (2) in (3), the total electric fields of the studied array consisting

of CP microstrip elements are given as

$$E_{T,\theta}(\theta, \varphi) = \sum_{n=1}^N E_{\theta}(\theta, \varphi_{en}) e^{j[\beta R \sin \theta \cos \varphi_{en} + \alpha_n]} \quad (4a)$$

$$E_{T,\varphi}(\theta, \varphi) = \sum_{n=1}^N E_{\varphi}(\theta, \varphi_{en}) e^{j[\beta R \sin \theta \cos \varphi_{en} + \alpha_n]}. \quad (4b)$$

For the RHCP and LHCP components of the electric fields (marked as E_{RHCP} and E_{LHCP}), they can be expressed as

$$E_{RHCP}(\theta, \varphi) = (\vec{e}_{\theta} - j\vec{e}_{\varphi})E_R \quad (5a)$$

$$E_{LHCP}(\theta, \varphi) = (\vec{e}_{\theta} + j\vec{e}_{\varphi})E_L. \quad (5b)$$

It is found that the magnitudes of the two components are $\sqrt{2}|E_R|$ and $\sqrt{2}|E_L|$, respectively. Based on (4) and (5), we have

$$E_R = [E_{T,\theta}(\theta, \varphi) + jE_{T,\varphi}(\theta, \varphi)]/2 \quad (6a)$$

$$E_L = [E_{T,\theta}(\theta, \varphi) - jE_{T,\varphi}(\theta, \varphi)]/2. \quad (6b)$$

Assuming that the input power of per CP element is P_0 , then the total power radiated by all antenna elements, ignoring the mutual coupling and the transmission loss, should be $N \cdot P_0$. Subsequently, the gains of the two CP components become [28]

$$G(\theta, \varphi)_{RHCP} = 20 \lg \left[\sqrt{2}|E_R| \sqrt{\frac{N \cdot P_0 \eta}{4\pi}} \right] \quad (7a)$$

$$G(\theta, \varphi)_{LHCP} = 20 \lg \left[\sqrt{2}|E_L| \sqrt{\frac{N \cdot P_0 \eta}{4\pi}} \right] \quad (7b)$$

where $\eta = 120\pi\Omega$. Finally, based on (1)–(7), the normalized gain of the studied array with sequentially rotated configuration can be calculated theoretically.

Here, a case study of the array including eight RHCP elements is carried out, where the radius of the ring array is $0.7 \lambda_0$. The radiation patterns of the array using the numerical model expressed in (1)–(7) are calculated for $l = -2, -1, 0$, and $+1$, as illustrated in Fig. 2(a). It should be noted that as studied in [28] and expressed in (2d), only the upper half-space result of the numerical model described in (1)–(7) is useful. It is found that RHCP waves are generated for these cases, while magnitude nulls are found for the copolarization except the case for $l = -1$. As for the case $l = -1$, the major lobe at the beam center reveals that the OAM mode l_{OAM} is zero based on the well-known knowledge as to the OAM-based waves [5]. On the other hand, a 3-D model of an array for full-wave simulation centered at 15 GHz is employed for phase-distribution analysis. The array consists of eight typically chamfered RHCP patches and uses same settings with the numerical model. Fig. 2(b) and (c) depicts the full-wave simulated radiation patterns and spatial phase distributions of the copolarized electric fields for the 3-D model. It is found in Fig. 2(a) and (b) that the main beams of the radiation patterns obtained from the numerical calculation and full-wave simulation are consistent. Moreover, spiral shapes are observed in Fig. 2(c) except the case for $l = 0$. This is completely different from the results for the array shown in Fig. 1(a) when $l = -1$, where a magnitude null is observed at the beam center

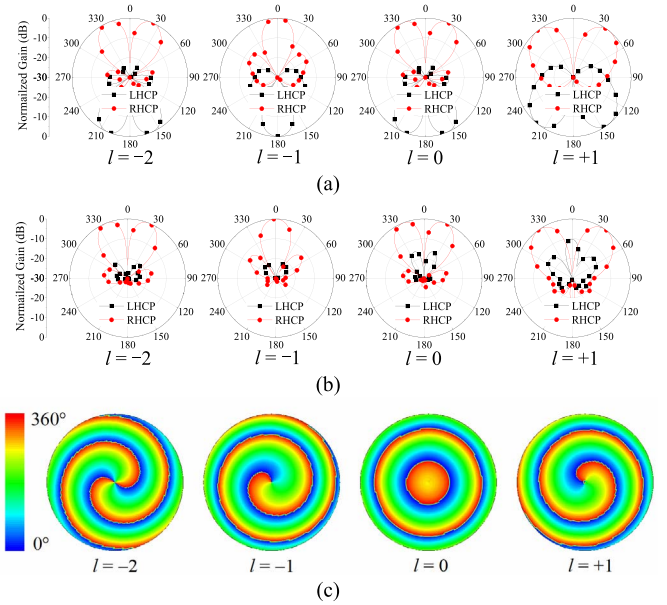


Fig. 2. (a) Calculated radiation patterns of the studied array using the numerical model illustrated in Fig. 1(b) and (1)–(7) at the xoz plane. (b) Full-wave simulated radiation patterns of the eight-element array using typically chamfered patch antennas at the xoz plane. (c) Full-wave simulated spatial phase distributions of the copolarized electric fields.

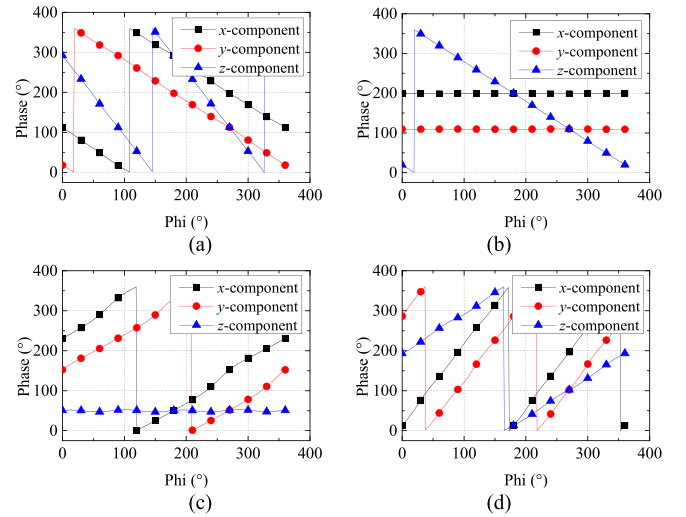


Fig. 3. Spatial phase distributions of the Cartesian components of the copolarized electric fields corresponding to the results of Fig. 2(c). (a) $l = -2$, (b) $l = -1$, (c) $l = 0$, and (d) $l = +1$.

and the OAM mode $l_{OAM} = -1$ [10], [11], [14]–[16], leading to the fact that helical phase fronts cannot be identified from the spiral shapes shown in Fig. 2(a) and (b). Furthermore, the spatial phase distributions of the Cartesian components of the electric fields around a circle perpendicular to the propagation direction for these cases are evaluated, as depicted in Fig. 3. It is seen that only the variations of z-components are consistent with those shown in Fig. 2(a) and (b). For the x- and y-components, the values of the variation periods are one less than those illustrated in Fig. 2(a) and (b).

It is known that for electromagnetic waves, the angular momentum (AM) consists of OAM and spin angular

TABLE I
COMPARISONS OF EXCITATION, AM, SAM, AND OAM MODES
IN THE STUDIED ARRAY CONSISTING OF CP AND LP
ELEMENTS ($N = 8, 12, 16$)

Element	l	j_{AM}	s	l_{OAM}	Array Polarization
LHCP element	-2	-2	+1	-3	LHCP
	-1	-1	+1	-2	LHCP
	0	0	+1	-1	LHCP
	+1	+1	+1	0	LHCP
	+2	+2	+1	+1	LHCP
RHCP element	-2	-2	-1	-1	RHCP
	-1	-1	-1	0	RHCP
	0	0	-1	+1	RHCP
	+1	+1	-1	+2	RHCP
	+2	+2	-1	+3	RHCP
LP element	-2	-2	-1	-1	RHCP
	-1	-1	-1	0	RHCP
	0	0	0	0	LP
	+1	+1	+1	0	LHCP
	+2	+2	+1	+1	LHCP

momentum (SAM), such that the AM mode $j_{AM} = l_{OAM} + s$, where s is the SAM mode. The SAM is associated with the polarization, and its mode is $-1, 0$, or $+1$ for RHCP, LP, or LHCP [5]. Based on this, it is reasonable to conclude that the difference between the z -component and the others described in Fig. 3 is due to the SAM, that is, the CPs. This means that the phase distributions of x - and y -components do not involve the SAM information and are only determined by the OAM. Hence, the OAM mode can be calculated on the basis of the definition that the OAM mode equals to the periodicity number of the spatial phase distribution of the electric fields when the SAM information has been removed [5]. Therefore, the OAM modes shown in Fig. 3 are $l_{OAM} = -1, 0, +1$, and $+2$ when $l = -2, -1, 0$, and $+1$, respectively. By involving the SAM mode information with the OAM modes, the AM modes are found to be $j_{AM} = -2, -1, 0$, and $+1$. That is to say, zero-OAM-mode waves are excited in spite of the helical shape observed from Fig. 2(a) and (b) for $l = -1$. Table I presents a comparison of the excitation mode l , AM mode j_{AM} , SAM mode s , OAM mode l_{OAM} , and spatial polarizations by using both the numerical and full-wave models. Note that three array models consisting of 8, 12, and 16 CP elements are analyzed, respectively, where the derived results are similar and summarized in Table I. It is matched with the typically nonsequentially rotated array that the same relationship for the OAM mode l_{OAM} and the element number N is observed, that is, $|l_{OAM}| < (N/2)$. The values of the excitation mode l equal to those of the AM mode j_{AM} , showing a simple difference compared with typical UCAs, where the excitation mode l is identified as the OAM mode l_{OAM} as described before. In Table I, the results of the array consisting of LP microstrip antennas with sequentially rotated configuration are also calculated and analyzed. For the LP-based array, only LHCP carrier can be generated when the

excitation mode $l > 0$, and RHCP for $l < 0$. Attractively, such restrictions do not exist when using the CP elements as listed in Table I, where polarizations and OAM modes are still independent.

Consequently, the helical phase fronts cannot be identified based on the observed spiral-shaped phase distributions for the CP radiations. When using the studied UCAs to generate OAM waves with the desired OAM modes l_{OAM} and CP radiations, the excitation mode should be set as $l = l_{OAM} + 1$ and $l = l_{OAM} - 1$ for LHCP and RHCP, respectively. In addition, it is found that for the studied scheme, nonzero-OAM-mode radiations can be obtained when all antenna elements are of the same excitation phases. Specifically, OAM modes of $l_{OAM} = -1$ and $l_{OAM} = +1$ are generated for LHCP and RHCP arrays, respectively. This means that there would be no extra phase shifters, resulting in simpler and potentially more compact configurations for the feeding networks compared with those of the typical UCAs. On the other hand, for the cases of the RHCP beams with OAM mode $l_{OAM} = +2, +3, \dots$, the phase shifters are essential based on the results. Note that the feeding networks of the sequentially rotated and nonsequentially rotated schemes have the same complexity when the state of $l_{OAM} = 0$ is considered. It is due to the fact that there would be no phase shifters for $l_{OAM} = 0$ in the nonsequentially rotated scheme. At this point, the phase shifters are essential in the sequentially rotated scheme. Therefore, the sequentially rotated scheme provides a potential way to simplify the feeding network for some specified OAM modes such as $l_{OAM} = +1$ for RHCP beams, but not for all OAM modes.

B. AR Bandwidths of the Studied Configuration

As for the studied UCAs, it is necessary to investigate the AR bandwidth at the beam maximum since phase fronts are different from those of the typical UCAs, as discussed earlier. Here, full-wave simulations are performed to show the AR bandwidths of the studied arrays. A typical circularly polarized microstrip antenna with a chamfered corner is considered as the array element. Several UCAs using the studied configuration shown in Fig. 1(b) with some different element numbers are constructed. The simulated radiation patterns and spatial phase distributions of these arrays agree well with the analyses presented earlier, thus not shown here for brevity. For the cases with different OAM modes, the maximal radiation directions should be different, thus here the AR performance for each case is calculated at the corresponding divergence angle. Note that in this paper, we focus on the comparisons among the cases using the sequentially and nonsequentially rotated configurations with the same OAM modes. There is no comparison between the cases with different OAM modes since the divergence angles are different. Fig. 4 illustrates the simulated AR bandwidths at the beam maximums against some element numbers N and excitation modes l . It is seen that the element number has little effect on AR bandwidth. Although the elements feature narrow AR bandwidths, the wide ones are found for the arrays except for the cases $l = 0$, as illustrated in Fig. 4(b). For performance

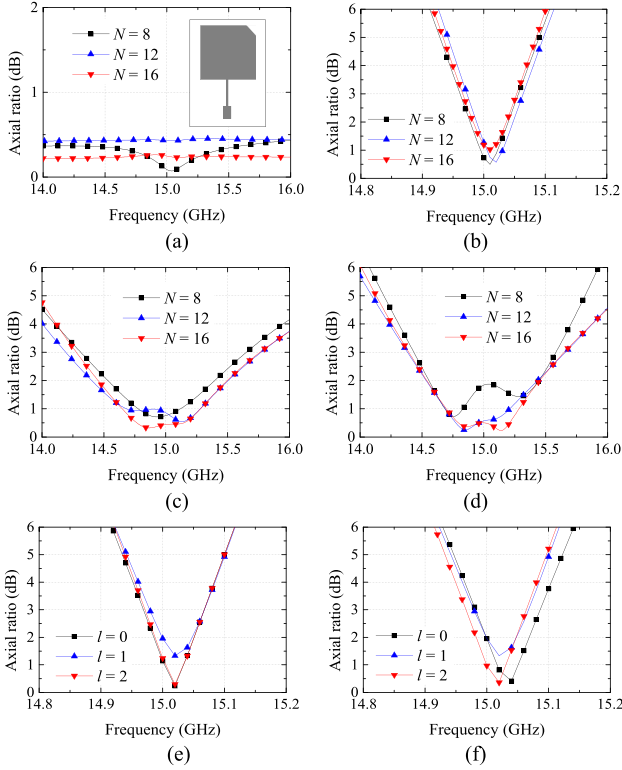


Fig. 4. Simulated ARs of the studied UCA consisting of chamfered RHCP microstrip antennas, where (a) $l = -1$, (b) $l = 0$, (c) $l = 1$, and (d) $l = 2$. Simulated results obtained from the typical arrays shown in Fig. 1(a), where (e) $N = 8$ and (f) $N = 16$.

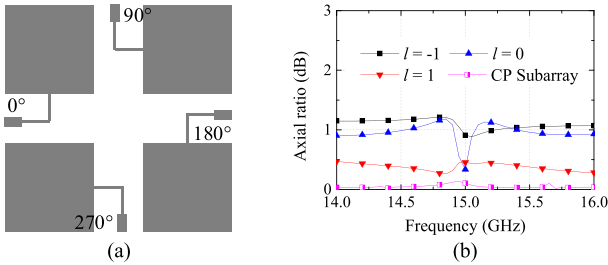


Fig. 5. (a) Configuration of an RHCP subarray using the sequentially rotated technique. (b) Simulated ARs of the sequentially rotated array using eight subarrays against with some excitation modes.

comparisons, Fig. 4(e) and (f) plot some simulated results at the beam maximums obtained from the arrays consisting of the chamfered patch antennas with nonsequentially rotated configuration, where narrow AR bandwidths are observed, and they are independent of the element number and excitation mode. Furthermore, an RHCP subarray shown in Fig. 5(a) is introduced as a single element of the studied UCA. The subarray radiates zero-OAM-mode RHCP waves with a wide AR bandwidth [29]. Fig. 5(b) presents the simulated ARs of the sequentially rotated array consisting of eight RHCP subarrays against some excitation modes. We can see that wide AR bandwidth is obtained including the case for $l = 0$. Also, similar performance can be observed by using LHCP elements and subarrays. From these discussions and compared with the nonsequentially rotated UCA, the studied sequentially rotated

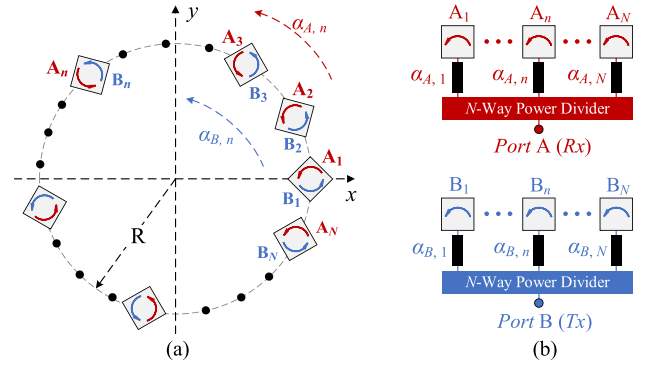


Fig. 6. Configurations of (a) proposed OAM-based CP array scenario for full-duplex applications and (b) its feeding network.

UCA can realize wide AR bandwidths at the beam maximum regardless of the AR bandwidth of the element.

III. OAM-BASED UCA SCENARIO FOR FULL-DUPLEX APPLICATIONS AND OAM-MODE SELECTION METHOD

As discussed earlier, the OAM-based communications are attractive for full-duplex systems, in terms of the interport isolation and further improvement in spectrum efficiency and data rate. Nevertheless, the suppression of the self-interference resulting from the mutual coupling among OAM-based antennas remains a challenge in practice. In this paper, an OAM-based CP array scenario for full-duplex applications is proposed based on the studied UCA, where the mutual couplings can be well suppressed, resulting in high interport isolations. Fig. 6 presents the configuration of the proposed scenario along with its feeding network. The array includes N elements that are sequentially rotated and positioned equidistantly around a ring. Each element includes two ports, corresponding to two same CP radiations. Based on this, a single element can be considered as a subarray composed of two antennas marked as A_n and B_n , where the subscript denotes the element number. Here, we classify all A-type antennas as array A, and the same classification for the array B. The feeding network includes two independent N -way power dividers with equal divisions and specified phase shifters for the two arrays. The feeding phases of the n th elements in arrays A and B are, respectively

$$\alpha_{A,n} = 2\pi l_A(n-1)/N \quad (8a)$$

$$\alpha_{B,n} = 2\pi l_B(n-1)/N \quad (8b)$$

where l_A and l_B are the excitation modes of the array A and array B, respectively.

As shown in Fig. 6(a), seeing that all elements (A_1 – A_N and B_1 – B_N) are of the same CP radiations, these may have strong mutual couplings among the elements due to the copolarization, especially the closer ones such as A_1 and B_1 , A_1 and B_2 . As a result, strong self-interference could be generated between subarray A and subarray B. In view of the reciprocity of ports A and B, we define the ports A and B as transmitting and receiving ports, respectively, to facilitate the analyses. By ignoring the influence of the feeding network and

considering the phase shifters to be lossless, the transmission response from the Tx to Rx is expressed as

$$S_{R_x, T_x} = M_A M_C M_B \quad (9)$$

where M_A and M_B are the feeding vectors for the Tx and Rx, respectively; M_C is an $N \times N$ coupling matrix including all coupling responses among antenna elements, given as

$$M_A = [e^{-j\alpha_{A,1}}, e^{-j\alpha_{A,2}}, \dots, e^{-j\alpha_{A,n}}, \dots, e^{-j\alpha_{A,N}}] \quad (10a)$$

$$M_B = [e^{-j\alpha_{B,1}}, e^{-j\alpha_{B,2}}, \dots, e^{-j\alpha_{B,n}}, \dots, e^{-j\alpha_{B,N}}]^T \quad (10b)$$

$$M_C = \begin{bmatrix} C_{A1,B1} & \cdots & C_{A1,BN} \\ \vdots & \ddots & \vdots \\ C_{AN,B1} & \cdots & C_{AN,BN} \end{bmatrix} \quad (10c)$$

where $C_{Am,Bn}$ denotes the coupling coefficient between the m th element in array A and the n th element in array B. Based on the coupling matrix, the transmission response from the Tx to Rx can be calculated by

$$S_{R_x, T_x} = S_1 + \cdots + S_n + \cdots + S_N \quad (11)$$

where

$$S_n = \sum_{k=1}^{N-n+1} C_{Ak, B(k+n-1)} e^{-j\alpha_{A,k}} e^{-j\alpha_{B, (k+n-1)}} + \sum_{k=N-n+2}^N C_{Ak, B(k-N+n-1)} e^{-j\alpha_{A,k}} e^{-j\alpha_{B, (k-N+n-1)}}. \quad (12)$$

Owing to the rotational symmetry, the relationship of the coupling coefficients can be expressed as

$$\begin{aligned} C_{A1, Bn} &= C_{A2, B(n+1)} = \cdots = C_{A(N-n+1), BN} \\ &= C_{A(N-n+2), B1} = C_{A(N-n+3), B2} = \cdots = C_{AN, B(N-1)}. \end{aligned} \quad (13)$$

In addition, from (8) we have

$$e^{-j\alpha_{B, (k+n-1)}} = e^{-j\alpha_{B, (k+n-1 \pm N)}}. \quad (14)$$

Consequently, (12) becomes

$$\begin{aligned} S_n &= \sum_{k=1}^N C_{A1, Bn} e^{-j\alpha_{A,k}} e^{-j\alpha_{B, (k+n-1)}} \\ &= C_{A1, Bn} e^{-j\frac{2\pi}{N} l_B (n-1)} \frac{1 - e^{-j2\pi(l_A + l_B)}}{1 - e^{-j\frac{2\pi}{N}(l_A + l_B)}}. \end{aligned} \quad (15)$$

Finally, the transmission responses from the Tx to Rx are

$$S_{R_x, T_x} = \sum_{n=1}^N C_{A1, Bn} e^{-j\frac{2\pi}{N} l_B (n-1)}, \quad l_A + l_B = 0 \quad (16a)$$

$$S_{R_x, T_x} = 0, \quad l_A + l_B \neq 0. \quad (16b)$$

One can see from (16b) that S_{R_x, T_x} would be zero when $l_A + l_B \neq 0$, leading to a response null for the transmission coefficient. This enables the self-interference resulting from the mutual couplings to be ideally suppressed under the mode-selection function of $l_A + l_B \neq 0$. As for (16a), owing to the complicated mutual coupling, it is reasonable to conclude that S_{R_x, T_x} would be nonzero when $l_A + l_B = 0$.

It should be mentioned that the result in (16b) is applicable to either the same or different CPs for arrays A and B, since the derivation of (8)–(16) is independent of the polarization. Moreover, the mutual couplings would be canceled even under the condition of $l_A = l_B$, indicating the suppression of the self-interference is still efficient for the Tx and Rx with the same OAM modes. At this point, the Tx and Rx are with the same OAM modes, leading to the same maximal beam angle in both the uplink and downlink. This is of great significance to improve the spectrum efficiency, and greatly different from some recent studies [6]–[8], where different OAM modes with same/dual polarizations are used to isolate the local Tx and Rx. Especially compared with the dual-polarized OAM scheme [7], the proposed architecture is more attractive since it is independent of the polarization. In the following, on-board prototypes at 15 GHz are developed and examined for demonstration purposes.

IV. DESIGN DESCRIPTIONS OF THE DEMONSTRATOR

The first work is to design the two-port antenna element. To generate two same CP radiations, a two-port subarray based on the sequentially rotated scheme is employed as the required two-port element. Here, dual-polarized microstrip antennas are used to construct the two-port subarray. In order to realize wide impedance bandwidths, the multilayer aperture-coupled configuration is introduced as shown in Fig. 7(a). The structure includes three stacked substrates, one patch, and one air layer. The air layer is positioned between the substrates 2 and 3. The patch is printed on the bottom of substrate 3. Feeding lines 1 and 2 are placed on the bottom of substrate 1 and the top of substrate 2, respectively. For each feeding line, an open-ended stub is loaded for impedance matching. A common ground with H-shaped slots for couplings between the feeding lines and the patch is inserted between the substrates 1 and 2.

Furthermore, a two-port subarray is constructed based on the dual-polarized antenna, as illustrated in Fig. 7(b). To radiate CP waves for the subarray, a typical feeding technique is the use of cascaded hybrids/T-junctions at the cost of bulky systems, as reported in [30] and [31]. In this paper, a series-fed power division network using compact open ring is utilized as the feeding network for each port of the subarray, as depicted in Fig. 7(b). The relative phases at the outputs of the power divider are anticlockwise with 0° , -90° , -180° , and -270° to generate RHCP waves for the subarray. Fig. 7(c) depicts the configuration of the proposed array using eight subarrays, including 16 ports marked from A_1 to A_8 for array A, and B_1 to B_8 for array B. The geometric parameters of the antenna element and the power divider are shown in Fig. 7(d) and (e) and Table II. A full-wave simulation of the proposed array is performed to show the self-interference resulting from the couplings among the antenna elements. Some simulated results are illustrated in Fig. 8, where the maximum coupling is approximately -19 dB at 15 GHz, corresponding to strong self-interference as analyzed earlier.

The feeding network, consisting of three-order power dividers based on T-junction with stepped multiple sections and specified phase shifters, is designed. The ideal model

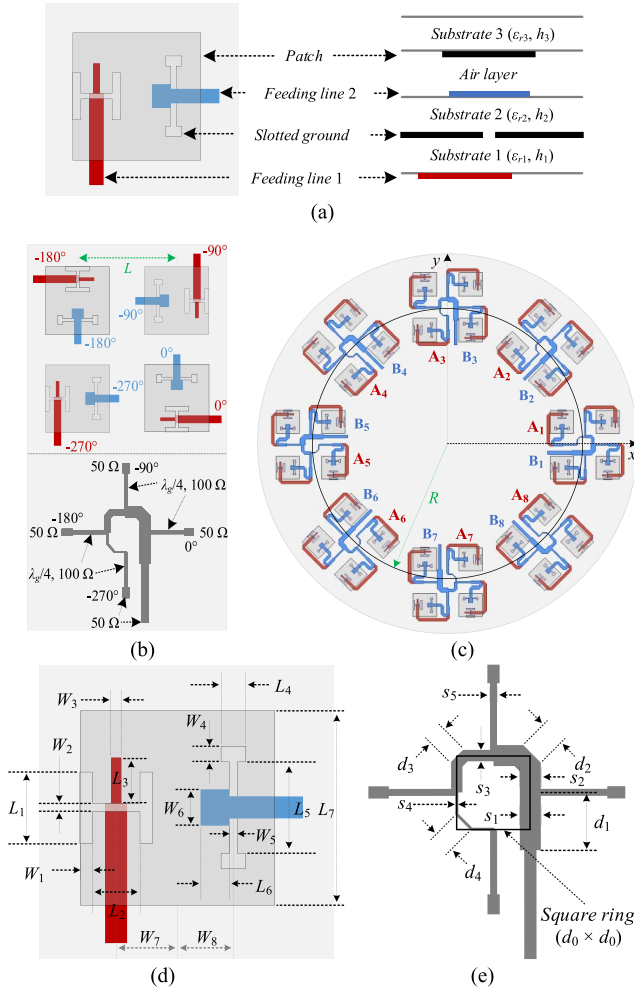


Fig. 7. (a) Geometric structure of the employed dual-polarized antenna. The relative permittivities (ϵ_r) and thicknesses (h) of the substrates are: $\epsilon_{r1} = 2.2$, $\epsilon_{r2} = 2.2$, $\epsilon_{r3} = 2.65$, $h_1 = 0.25$ mm, $h_2 = 0.25$ mm, and $h_3 = 1$ mm. (b) Configurations of the two-port CP subarray with its feeding network. (c) Configuration of the proposed array consisting of eight subarrays. The radius of the proposed array is $R = 1.8 \lambda_0$, where λ_0 is the free-space wavelength at 15 GHz. Geometric parameters of (d) dual-polarized antenna and (e) open-ring power divider, where the values are listed in Table II.

TABLE II

GEOMETRIC PARAMETERS OF THE ANTENNA AND FEEDING NETWORK

Antenna element (mm)				Feeding network (mm)					
L_1	2.25	L_6	0.89	W_4	0.47	s_1	1.20	d_1	3.30
L_2	1.50	L_7	6.13	W_5	0.26	s_2	1.20	d_2	1.42
L_3	1.42	W_1	0.40	W_6	1.13	s_3	0.65	d_3	0.96
L_4	0.72	W_2	0.24	W_7	1.95	s_4	0.17	d_4	1.27
L_5	2.90	W_3	0.32	W_8	1.73	s_5	0.40	-	-

of the three-order power divider is depicted in Fig. 9(a), where the electric length (referring to $f_0 = 15$ GHz) of a_i ($i = 1, \dots, K$) corresponds to the required excitation phase described in (8). The transmission coefficient from port 1 to port $(k + 1)$ th ($k = 1, \dots, K$) in the power divider versus frequency f can be expressed as

$$S_{k+1,1} = (S_{PD})^3 e^{-j\alpha_k f / f_0} \quad (17)$$

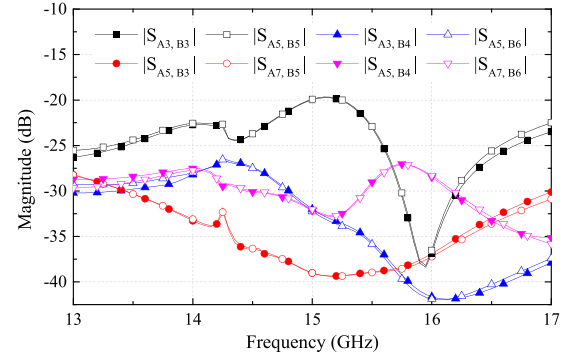


Fig. 8. Simulated couplings between some elements of array A and array B.

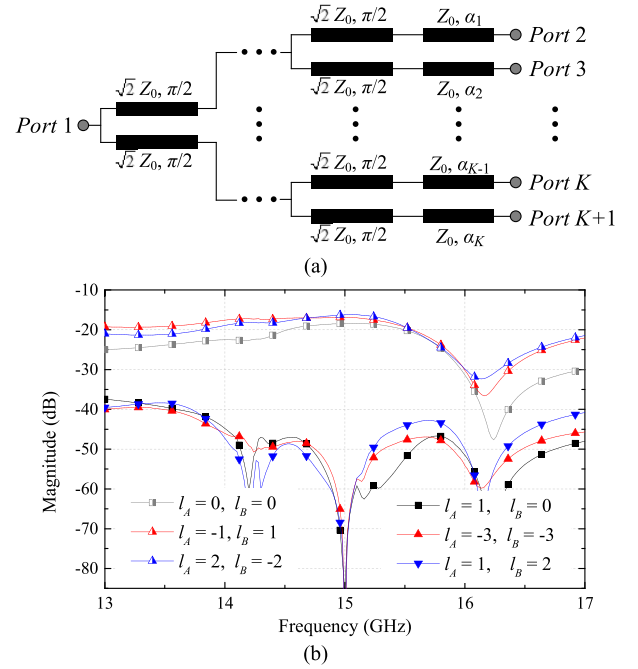


Fig. 9. (a) Schematic of a T-junction-based power divider with specified phase shifters as the feeding structures for the proposed array. (b) Calculated transmission responses between the Tx and Rx of the proposed array using several groups of the excitation modes.

where S_{PD} is the transmission coefficient of a single T-junction. As shown in Fig. 9(a), the transmission response between the Tx and Rx of the proposed OAM-based array can be calculated on the basis of (9), (10), and (17). For the coupling coefficients recorded in (10c), they are determined by the full-wave simulations. The calculated results of the transmission response with several groups of excitation modes l_A and l_B are depicted in Fig. 9(b). It is clearly seen that based on the mode-selection equation (16b), the self-interference due to the strong mutual couplings among the antenna elements can be well suppressed within a wide frequency band referring to an in-port isolation of 40 dB. At the center frequency 15 GHz, response nulls are found, showing perfectly self-interference cancellations. Particularly, for the case of $l_A = l_B = -3$, the self-interference can be well canceled when Tx and Rx are operated at the same OAM mode of $l_{OAM} = -2$, as discussed earlier. For performance comparisons, responses

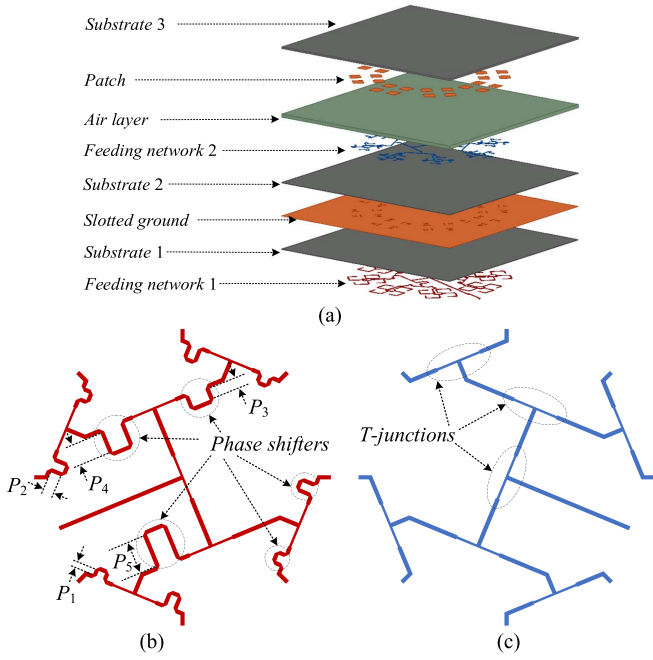


Fig. 10. (a) 3-D view of the demonstrator. Layouts of (b) feeding network 1 and (c) feeding network 2. The dimensions are (unit: millimeters): $P_1 = 0.90$, $P_2 = 1.84$, $P_3 = 1.87$, $P_4 = 3.65$, and $P_5 = 5.51$.

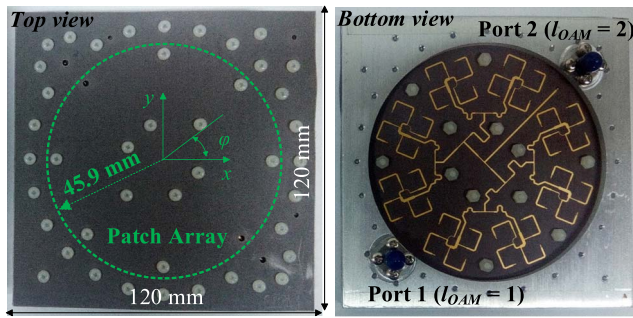


Fig. 11. Photographs of the fabricated demonstrator.

for the modes that are not consistent with (16b) are also presented, where it is clearly seen the isolations are less than 20 dB at 15 GHz.

To this end, prototypes centered at 15 GHz are developed and fabricated based on the architectures shown in Figs. 6 and 7, where the excitation modes are $l_A = +1$ and $l_B = 0$. The corresponding OAM modes are, respectively, $l_{OAM} = +2$ and $l_{OAM} = +1$ based on the above-mentioned discussion. The 3-D view of the demonstrator and the layout of its feeding networks are described in Fig. 10. The full-wave simulated results and measurements are described as follows.

V. MEASUREMENTS OF THE DEVELOPED DEMONSTRATOR

The fabricated demonstrator is further assembled, as pictured in Fig. 11, where a metal jig is used for supporting purposes. The overall size of the demonstrator is 120 mm \times 120 mm, and the outside radius of the patch array is 45.9 mm.

Fig. 12 depicts the measured impedance matching performance and transmission response between the two ports of

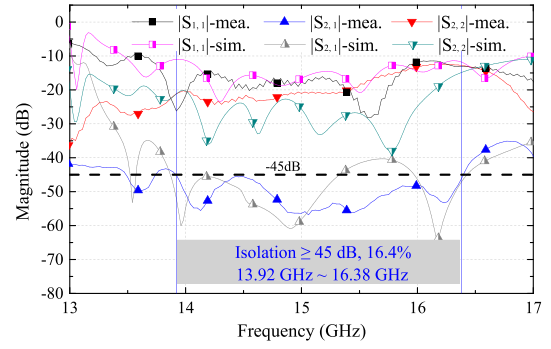


Fig. 12. Measured and simulated isolation and impedance matching responses.

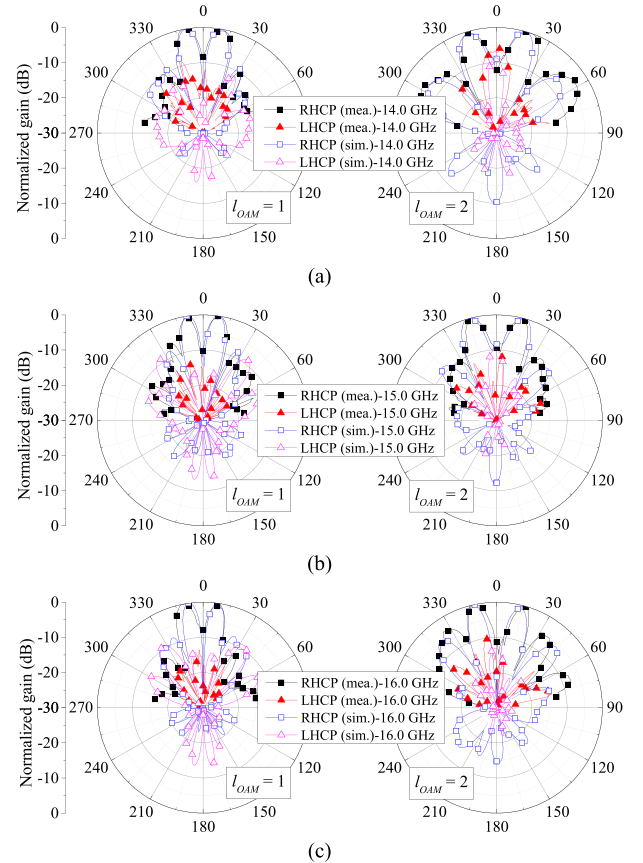


Fig. 13. Measured and simulated far-field radiation patterns of the demonstrator.

the demonstrator. It is seen that the impedance bandwidths referring to $|S_{1,1}| \leq -10$ dB are over 3.8 GHz (from 13.2 to beyond 17.0 GHz) and over 4.0 GHz (from 13.0 to beyond 17.0 GHz) for ports 1 and 2, respectively. The relative isolation bandwidth is 16.4% (13.92–16.38 GHz) referring to a 45 dB level, exhibiting high self-interference suppressions. Hence, the isolation bandwidths are fully covered by the impedance bandwidths of the two ports. The far-field radiation patterns at 14.0, 15.0, and 16.0 GHz are measured and illustrated in Fig. 13. One can see that RHCP waves are excited, and the central magnitude nulls are observed for all cases, which is consistent with the analyses in Section II. For $l_{OAM} = +1$

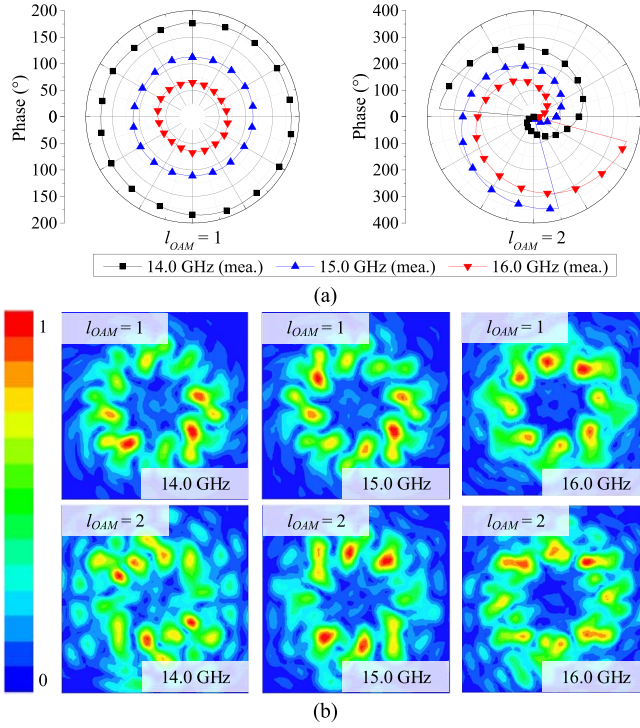


Fig. 14. (a) Measured spatial phase distributions of the copolarized electric fields. (b) Simulated distributions of normalized magnitude of instantaneous near-zone electric fields.

and $l_{OAM} = +2$ at 15.0 GHz, the measured peak gains are approximately 17.3 and 13.5 dBi with the directions of 9° and 14° , respectively. The angles of the maximal beam at 14, 15, and 16 GHz are within the range of $8^\circ - 10^\circ$ when $l_{OAM} = +1$, and the corresponding 3 dB beamwidths are approximately 10° . As for the case $l_{OAM} = +2$, the corresponding angles are within $13^\circ - 16^\circ$, and the 3 dB beamwidths are approximately 11° .

The simulated spatial phase distributions for the demonstrator are identical with those described in Fig. 2(a) and (b), thus they are not detailed here for brevity. In order to measure the phase distributions of the copolarized electric fields, circles across boresight directions and $20 \lambda_0$ away from the demonstrator are employed. The measured results are shown in Fig. 14. For the case of $l_{OAM} = +1$, there are no helical shapes, indicating the AM modes are zero due to the RHCP radiations as discussed earlier. As for the case of $l_{OAM} = +2$, it is found that spiral phase fronts of the copolarized electric fields are obtained corresponding to an AM mode $j_{AM} = +1$ since the spatial phase increases anticlockwise by one period within a circle. The simulated amplitude distributions are also presented as shown in Fig. 14(b). Despite without the measurements due to the lack of 3-D test environment, good agreement between simulations and measurements for the radiation patterns and phase distributions could make us reasonably perceive the consistency of the amplitude distributions. On the other hand, the AR performances at the beam maximums corresponding to 15.0 GHz are also measured, as shown in Fig. 15. It is clearly seen that wide AR bandwidths are observed for both ports. Note that in the light of our

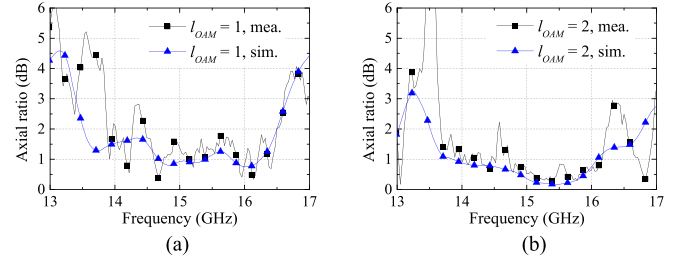


Fig. 15. Measured and simulated ARs of the demonstrator at the maximal radiation directions referring to 15.0 GHz.

TABLE III
MEASURED AND CALCULATED AZIMUTH SPECTRUM
OF THE DEVELOPED ANTENNA ARRAY

Measured ω_m	Port 1 ($l_{OAM} = +1, \theta = 9^\circ$)			Port 2 ($l_{OAM} = +2, \theta = 14^\circ$)		
	OAM mode	14 GHz	15 GHz	16 GHz	14 GHz	15 GHz
0	0.042	0.007	0.003	0.044	0.007	0.006
+1	0.577	0.582	0.578	0.048	0.052	0.050
+2	0.042	0.007	0.003	0.461	0.477	0.481
+3	0.001	0.007	0.016	0.052	0.050	0.050
Calculated ω_m	Port 1 ($l_{OAM} = +1, \theta = 9^\circ$)			Port 2 ($l_{OAM} = +2, \theta = 14^\circ$)		
OAM mode	14GHz	15GHz	16GHz	14GHz	15GHz	16GHz
0	0	0	0	0	0	0
+1	0.580	0.582	0.579	0	0	0
+2	0	0	0	0.470	0.483	0.487
+3	0	0	0	0	0	0

analysis, the wide AR bandwidths result from the sequentially rotated array configuration for the case of $l_{OAM} = +2$, but for $l_{OAM} = +1$, they are attributed to the 2×2 subarray.

Due to the practical errors/tolerances, it might not be possible to generate a pure OAM mode, and the desired OAM mode could be contaminated by other parasitic OAM modes. Therefore, the OAM mode purity of the developed antenna array is also analyzed. Specifically, the azimuth spectrum ω_m , representing the weight of the OAM m -mode in the OAM beam with the desired OAM mode of l_{OAM} , is measured. As discussed in [11] that for the OAM beams generated by using circular antenna arrays, the azimuth spectrum can be obtained by

$$\omega_m = \frac{1}{2\pi} \int_0^{2\pi} S(\theta, \varphi) e^{-jm\varphi} d\varphi \quad (18)$$

where $S(\theta, \varphi)$ is the array factor described in (3). It is seen that the azimuth spectrum is a function of θ and φ . As we discussed earlier that since we focus on the performance at the maximal radiation directions at the center frequency, the divergence angles are set as $\theta = 9^\circ$ and $\theta = 14^\circ$ for the cases of $l_{OAM} = +1$ and $l_{OAM} = +2$, respectively. The experimental results of the azimuth spectrum are listed in Table III. On the other hand, the ideal results of using numerical calculations are also provided, where the azimuth spectrum is

TABLE IV
PERFORMANCE COMPARISONS AMONG SOME PUBLISHED
AND THE PROPOSED FULL-DUPLEX SCHEMES

Refs./Years	[4]/2017	[7]/2017	[32]/2018	This work
Isolation methods	Polarization-based	OAM-based	Polarization-based	OAM-based
Isolation (dB) & frequency (GHz)	≥ 70 2.38–2.43	≥ 25 5.4–5.6	≥ 32 11.0–15.5	≥ 45 13.92–16.38
Polarizations of Tx and Rx	Orthogonal LPs	Orthogonal LPs	Orthogonal LPs	Same CPs
Antenna configurations	Single element	2×2 Array	2×2 Array	Ring array (4×8)
Potential of multi-links for Tx and Rx	No	No	No	Yes

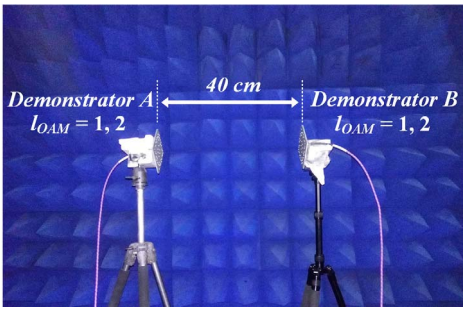


Fig. 16. Photograph of the experimental installation for transmission experiments.

expressed as [11]

$$\omega_m = \frac{1}{2\pi} \int_0^{2\pi} e^{-j l_{OAM} \phi} J_{l_{OAM}}(2\pi R \sin \theta / \lambda_0) e^{-j m \phi} d\phi \quad (19)$$

where $J_{l_{OAM}}$ is the Bessel function of the first kind, with the order of l_{OAM} and the variable of $(2\pi R \sin \theta / \lambda_0)$. It can be found from Table III that the good agreement between the measured and calculated results is observed, exhibiting a good OAM mode purity for the developed array. Moreover, for the cases of $l_{OAM} = +1$ and $l_{OAM} = +2$, the values of the azimuth spectrum corresponding to the desired OAM mode are approximately 0.58 and 0.47, respectively. These values are close to those obtained from the array using non-sequentially rotated configuration, which are correspondingly around 0.6 and 0.5 as analyzed in [11]. The above-mentioned discussion indicates that the OAM beams obtained from the proposed array feature good OAM mode purity, and there is no distinct difference for the azimuth spectrum compared with the typically nonsequentially rotated array.

Furthermore, transmission experiments are carried out to show the transmission characteristics between links with different OAM modes. As shown in Fig. 16, the experiment scenario is composed of two copies of the developed demonstrator placed face-to-face. Specifically, the transmission distance is 40 cm, shorter than the Rayleigh distance in view of the discussion that the OAM-based transmission is feasible within a few Rayleigh distances [6], [8], [11], [20]. The measured transmission coefficients are shown in Fig. 17. The normalized isolation between the matched and mismatched OAM-based

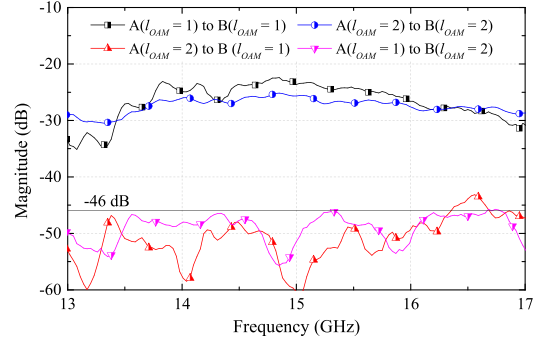


Fig. 17. Measured transmission coefficients between the two demonstrators.

links in Fig. 17 is nearly 20 dB within the frequency range of 14–16 GHz, and higher than 25 dB around the center frequency of 15 GHz. Referring to the recent studies on OAM-based wireless communications, a crosstalk level of approximately 20 dB among different OAM links could enable the reliable communications. Based on the discussion, it can be concluded that the measured results shown in Fig. 17 exhibit a well-designed orthogonality between the transmission links under different OAM modes. Note that here the received power for $l_{OAM} = +2$ is approximately 2 dB lower than that for $l_{OAM} = +1$ around 15 GHz. This is consistent with the results reported in [8] and [11]. For performance comparisons, Table IV summarizes the performance of the proposed scheme in this paper and some reported studies for full-duplex applications. As we can see that the developed demonstrator exhibits a high interport isolation with passive operation at Ku-band, where both Tx and Rx are of the same CPs. Moreover, since the proposed architecture is independent of polarizations, it exhibits the potential for multilink full-duplex applications to further improve the spectrum efficiency and data rate, which can be achieved by simply expanding the proposed architecture to more rings. In short, the proposed OAM array behaves good antiinterference ability for each link and potential enhancement for the system capacity under the same CP carriers as well as high interport isolations between the local Tx and Rx.

VI. CONCLUSION

OAM-based UCA using sequentially rotated CP microstrip antennas is studied in this paper. The relationship between OAM modes and phase settings of the array elements are analyzed. Results reveal that for the studied UCA, the excitation mode is not the OAM mode but the AM mode for the generated OAM waves. This is completely different from the results for the UCAs without using the sequentially rotated configuration, and of great significance for designing such kinds of UCA with desired OAM modes. Based on the studied UCA, nonzero-OAM-mode waves can be generated even all antenna elements are excited with the same phases. It is also found that wide AR bandwidths at the beam maximum can be realized for the studied UCA, regardless of the AR bandwidth of the element. Furthermore, based on the studied UCA, a dual-OAM-mode circularly polarized scenario is proposed for full-duplex applications. Studies indicate that the

self-interference resulting from the strong mutual couplings among antenna elements can be ideally canceled theoretically by using the proposed OAM-mode selection method. For verification purposes, a Ku-band prototype by using sharing-antenna scheme is developed, fabricated, and measured. Experimental results match well with the theoretical and simulated results.

REFERENCES

- [1] Y.-S. Choi and H. Shirani-Mehr, "Simultaneous transmission and reception: Algorithm, design and system level performance," *IEEE Trans. Wireless Commun.*, vol. 12, no. 12, pp. 5992–6010, Dec. 2013.
- [2] J. Wu, M. Li, and N. Behdad, "A wideband, unidirectional circularly polarized antenna for full-duplex applications," *IEEE Trans. Antennas Propag.*, vol. 66, no. 3, pp. 1559–1563, Mar. 2018.
- [3] M. Heino, S. N. Venkatasubramanian, C. Icheln, and K. Haneda, "Design of wavetraps for isolation improvement in compact in-band full-duplex relay antennas," *IEEE Trans. Antennas Propag.*, vol. 64, no. 3, pp. 1061–1070, Mar. 2016.
- [4] H. Nawaz and I. Tekin, "Dual-polarized, differential fed microstrip patch antennas with very high interport isolation for full-duplex communication," *IEEE Trans. Antennas Propag.*, vol. 65, no. 12, pp. 7355–7360, Dec. 2017.
- [5] B. Thidé *et al.*, "Utilization of photon orbital angular momentum in the low-frequency radio domain," *Phys. Rev. Lett.*, vol. 99, no. 8, p. 087701, Aug. 2007.
- [6] Y. Yan *et al.*, "High-capacity millimetre-wave communications with orbital angular momentum multiplexing," *Nature Commun.*, vol. 5, p. 4876, Mar. 2014.
- [7] H. Li, L. Kang, F. Wei, Y.-M. Cai, and Y.-Z. Yin, "A low-profile dual-polarized microstrip antenna array for dual-mode OAM applications," *IEEE Antennas Wireless Propag. Lett.*, vol. 16, pp. 3022–3025, 2017.
- [8] Y. Ren *et al.*, "Line-of-sight millimeter-wave communications using orbital angular momentum multiplexing combined with conventional spatial multiplexing," *IEEE Trans. Wireless Commun.*, vol. 16, no. 5, pp. 3151–3161, May 2017.
- [9] W.-Y. Huang, J.-L. Li, H.-Z. Wang, J.-P. Wang, and S.-S. Gao, "Vortex electromagnetic waves generated by using a ladder spiral phase plate and a microstrip antenna," *Electromagnetics*, vol. 36, no. 2, pp. 102–110, 2016.
- [10] M. Lin, Y. Gao, P. Liu, and J. Liu, "Theoretical analyses and design of circular array to generate orbital angular momentum," *IEEE Trans. Antennas Propag.*, vol. 65, no. 7, pp. 3510–3519, Jul. 2017.
- [11] Y. Gong *et al.*, "Generation and transmission of OAM-carrying vortex beams using circular antenna array," *IEEE Trans. Antennas Propag.*, vol. 65, no. 6, pp. 2940–2949, Jun. 2017.
- [12] M. Tamagnone, C. Craeye, and J. Perruisseau-Carrier, "Comment on 'Encoding many channels on the same frequency through radio vorticity: First experimental test,'" *New J. Phys.*, vol. 14, no. 11, p. 118001, Nov. 2012.
- [13] O. Edfors and A. J. Johansson, "Is orbital angular momentum (OAM) based radio communication an unexploited area?" *IEEE Trans. Antennas Propag.*, vol. 60, no. 2, pp. 1126–1131, Feb. 2012.
- [14] X. Bai, X. Liang, R. Jin, and J. Geng, "Generation of OAM radio waves with three polarizations using circular horn antenna array," in *Proc. 9th Eur. Conf. Antennas Propag. (EUCAP)*, Lisbon, Portugal, Aug. 2015, pp. 1–4.
- [15] X. Sun, Y. Du, Y. Fan, and M. Sun, "The design of array antenna based on multi-modal OAM vortex electromagnetic wave," in *Proc. PIERS*, Shanghai, China, Nov. 2016, pp. 2786–2791.
- [16] Q. Liu, Z. N. Chen, Y. Liu, F. Li, Y. Chen, and Z. Mo, "Circular polarization and mode reconfigurable wideband orbital angular momentum patch array antenna," *IEEE Trans. Antennas Propag.*, vol. 66, no. 4, pp. 1796–1804, Apr. 2018.
- [17] C. Deng, W. Chen, Z. Zhang, Y. Li, and Z. Feng, "Generation of OAM radio waves using circular Vivaldi antenna array," *Int. J. Antennas Propag.*, vol. 2013, Art. no. 847859.
- [18] Y.-M. Zhang and J.-L. Li, "Comments on 'radial uniform circular antenna array for dual-mode OAM communication,'" *IEEE Antennas Wireless Propag. Lett.*, vol. 17, no. 4, pp. 719–721, Apr. 2018.
- [19] L. Li and X. Zhou, "Mechanically reconfigurable single-arm spiral antenna array for generation of broadband circularly polarized orbital angular momentum vortex waves," *Sci. Rep.*, vol. 8, Mar. 2018, Art. no. 5128.
- [20] W. Zhang *et al.*, "Mode division multiplexing communication using microwave orbital angular momentum: An experimental study," *IEEE Trans. Antennas Propag.*, vol. 16, no. 2, pp. 1308–1318, Feb. 2017.
- [21] H. Tian, Z. Liu, W. Xi, G. Nie, L. Liu, and H. Jiang, "Beam axis detection and alignment for uniform circular array-based orbital angular momentum wireless communication," *IET Commun.*, vol. 10, no. 1, pp. 44–49, 2016.
- [22] C. Deng, K. Zhang, and Z. Feng, "Generating and measuring tunable orbital angular momentum radio beams with digital control method," *IEEE Trans. Antennas Propag.*, vol. 65, no. 2, pp. 899–902, Feb. 2017.
- [23] M. L. N. Chen, L. J. Jiang, and W. E. I. Sha, "Detection of orbital angular momentum with metasurface at microwave band," *IEEE Antennas Wireless Propag. Lett.*, vol. 17, no. 1, pp. 110–113, Jan. 2018.
- [24] M. Oldoni *et al.*, "Space-division demultiplexing in orbital-angular-momentum-based MIMO radio systems," *IEEE Trans. Antennas Propag.*, vol. 63, no. 10, pp. 4582–4587, Oct. 2015.
- [25] Y. Hu, S. Zheng, Z. Zhang, H. Chi, X. Jin, and X. Zhang, "Simulation of orbital angular momentum radio communication systems based on partial aperture sampling receiving scheme," *IET Microw., Antennas Propag.*, vol. 10, no. 10, pp. 1043–1047, 2016.
- [26] W. Zhang, S. Zheng, Y. Chen, X. Jin, H. Chi, and X. Zhang, "Orbital angular momentum-based communications with partial arc sampling receiving," *IEEE Commun. Lett.*, vol. 20, no. 7, pp. 1381–1384, Jul. 2016.
- [27] T. D. Drysdale, B. Allen, and C. Stevens, "Discretely-sampled partial aperture receiver for orbital angular momentum modes," in *Proc. IEEE APS Int. Symp.*, Jul. 2017, pp. 951–952.
- [28] W. L. Stutzman and G. A. Thiele, *Antenna Theory and Design*, 3rd ed. New York, NY, USA: Wiley, 2012.
- [29] J. Huang, "A technique for an array to generate circular polarization with linearly polarized elements," *IEEE Trans. Antennas Propag.*, vol. AP-34, no. 9, pp. 1113–1124, Sep. 1986.
- [30] A. B. Smolders, R. M. C. Mestrom, A. C. F. Reniers, and M. Geurts, "A shared aperture dual-frequency circularly polarized microstrip array antenna," *IEEE Antennas Wireless Propag. Lett.*, vol. 12, pp. 120–123, 2013.
- [31] J. Ha, M. A. Elmansouri, P. V. Prasannakumar, and D. S. Filipovic, "Monostatic co-polarized full-duplex antenna with left- or right-hand circular polarization," *IEEE Trans. Antennas Propag.*, vol. 65, no. 10, pp. 5103–5111, Oct. 2017.
- [32] W. Wang, J. Wang, A. Liu, and Y. Tian, "A Novel broadband and high-isolation dual-polarized microstrip antenna array based on quasi-substrate integrated waveguide technology," *IEEE Trans. Antennas Propag.*, vol. 66, no. 2, pp. 951–956, Feb. 2018.



Yi-Ming Zhang (S'17) received the M.S. degree from the School of Physical Electronics, University of Electronic Science and Technology of China, Chengdu, China, in 2014, where he is currently pursuing the Ph.D. degree.

His current research interests include MIMO antenna decoupling and single-channel full-duplex communications, and antenna-based and analog-based self-interference suppressions.



Jia-Lin Li received the M.S. degree in electronic engineering from the University of Electronic Science and Technology of China (UESTC), Chengdu, China, in 2004, and the Ph.D. degree in electronic engineering from the City University of Hong Kong, Hong Kong, in 2009.

From 2005 to 2006, he was a Research Associate with the Wireless Communication Research Center, City University of Hong Kong. Since 2009, he has been with the School of Physical Electronics, UESTC, where he is currently a Professor. His current research interests include microwave/millimeter-wave antenna and arrays, circuits and systems, interactions between microwave and complex medium, and so on.